A Compact Scalable Circuit Model for RF MEMS Switches

H.M.R. Suy*, H.G.A. Huizing*, P.G. Steeneken* and O.I. Yanson**

* NXP Semiconductors Research Laboratories, High Tech Campus 5
5656 AE Eindhoven, The Netherlands, hilco.suy@nxp.com
** NXP Semiconductors Innovation Center RF, Gerstweg 2
6534 AE Nijmegen, The Netherlands

ABSTRACT

A compact circuit model for RF MEMS switches is presented. The model is 1D and scalable, apart from two model factors that take into account higher-order physical effects. The model consists of six parameters that can easily be extracted from CV measurements. In addition, a separate parasitic network is developed that can be coupled to our compact switch model. The model is verified in CV, transient, and S-parameter measurements, and is used in a wide range of numerical simulations, such as envelope and harmonic balance.

Keywords: RF switches, MEMS switches, RF MEMS, compact model, circuit model.

1 INTRODUCTION

For the purpose of IC and system design, circuit simulators require compact and accurate electromechanical models of RF MEMS switches. In literature, a clear distinction can be made between one-dimensional (1D, with a single mechanical state variable) and multi-dimensional (MD) analytical models. Although 1D models are easy to use, existing models lack accuracy, when compared to Finite Element Method simulations or measurements. MD models, on the other hand, are in general more accurate, but computationally less efficient.

Table 1 shows an overview of published 1D and MD models. It can be observed that most models concentrate on the thorough description of a few physical phenomena that are observed in RF MEMS switches. Experimental verification is infrequently addressed. In this paper it is our intention to present a model that: (i) includes a wide range of physical phenomena, (ii) is computationally efficient (compact) and suitable for a variety of simulation analyses, (iii) can easily be implemented in circuit simulators (written in Verilog-A), (iv) allows for straightforward parameter extraction, (v) is extensively numerically tested and validated on measurements. In section 2, our 1D model will be discussed, followed by simulations and measurements in section 3.

2 RF MEMS SWITCH MODEL

The free-body diagram of an RF MEMS switch is schematically shown in figure 1. The switch consists

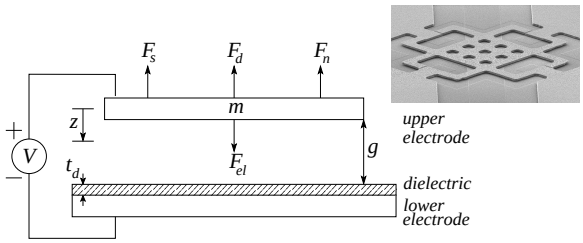

Figure 1: Free-body diagram of the model of the RF MEMS switch. Inset: SEM image of a switch [12].

of a perforated upper electrode with mass m, which is suspended by springs over a lower electrode, separated by an airgap g, and dielectric with thickness t_d. The vertical displacement from the initial gap g is called z. The membrane is subject to an electrostatic force F_{el}, a spring force F_s, and a damping force F_d. In addition, when the switch is closed, a contact or normal force F_n is generated. The voltage that is applied between the upper and lower electrode equals V.

Applying Newton's second law of motion, the equation of motion can be written in terms of the single state variable z of the lumped mass m:

$$\sum F = F_{el} - F_s - F_d - F_n = F_i = m\frac{d^2z}{dt^2}\,, \qquad (1)$$

with inertial force F_i. In the next subsections, the individual terms that form this 1D model, will be discussed.

2.1 Electrostatic Force

The electrostatic force on a voltage-driven device is:

$$F_{el} = \frac{1}{2}V^2\frac{dC_{tot}}{dz}\,. \qquad (2)$$

Often, the parallel plate capacitance C_{pp} is used as an approximation of the total capacitance C_{tot}. However, for structures with lateral dimensions in the same order of magnitude as the gap between the surfaces, fringing electrostatic fields come into play. In this research, see figure 2, fringing capacitance contributions arise from the side wall of the upper electrode (finite thickness) along the outer edge (C''_{sw}) and the edges of the perforations (C'_{sw}). Furthermore, since the upper electrode has finite length, extra capacitance contributions C''_b and C'_b can be defined for the outer edge and perforation

Table 1: Literature overview of analytical 1D and MD RF MEMS switch models, compared to the 1D model presented in this paper. In the case where the model analysis is supported by measurement results, the symbol (m) is added.

		1D models							MD models				This paper (1D)
		[1]	[2]	[3]	[4]	[5]	[6]	[7]	[8]	[9]	[10]	[11]	
Included physics	Squeeze film damping												
	analytical, scalable damping coefficient	x		x			x	x	x	x			**x**
	numerical damping coefficient		x								x		
	Fringing electrostatic fields					x				x		x	**x**
	Contact force model			x			x		x				**x**
	Membrane bending (partial-release)								x	x	x	x	**x**
	Parasitic network	x			x								**x**
Analysis types	DC												
	full hysteretic behavior								x(m)				**x(m)**
	(up to) pull-in only		x		x	x				x		x	
	Transient (opening & closing)	x	x(m)	x			x	x(m)	x(m)	x	x(m)		**x(m)**
	S-parameters	x			x						(m)		**x(m)**
	Envelope (large signal RF)												**x**
	Harmonic balance												**x**

edges, respectively. The contribution of the top of the membrane is numerically found to be negligibly small.

Analytical expressions are identified separately with

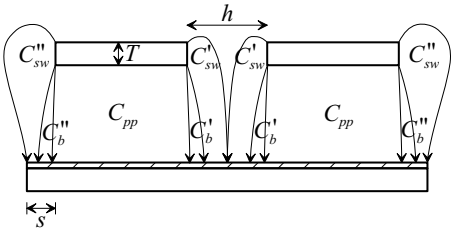

Figure 2: Cross-section of a MEMS with one square perforation, with the schematic representation of the fringing electrostatic fields. The dimension of the perforation is h x h, the upper electrode thickness is T, and the upper and lower electrode spacing equals s.

conformal mapping techniques for the finite length and finite thickness effect, for a 2D situation with a planar *infinite* ground electrode [13], [14]. Two fringing parameters are introduced to take into account the 3D effects of the perforations (C_b' and C_{sw}') and the finite *ground* electrode (C_b'' and C_{sw}''). The parameters are set-up as cubic Response Surface Models (RSM) and are found to be valid in the ranges:

$$\frac{g}{T} \in \begin{bmatrix} 0 & 1.8 \end{bmatrix}, \frac{h}{T} \in \begin{bmatrix} 2.5 & 20 \end{bmatrix}, \frac{s}{T} \in \begin{bmatrix} 1/3 & 3 \end{bmatrix}, \quad (3)$$

covering a wide range of practical devices. By choosing this approach instead of creating an RSM for the total capacitance C_{tot}, a higher degree of scalability is attained. The accuracy of this fringing model is validated by numerical 3D EM simulations (figure 3).

2.2 Spring and Damping Force

The spring force, with linear spring stiffness k, of a crableg configuration with one rigidly fixed end (anchor) and one end with only vertical freedom of motion (guided-end) is given in [15]. Squeeze-film damping is modeled analytically and scalable, as given in [16],

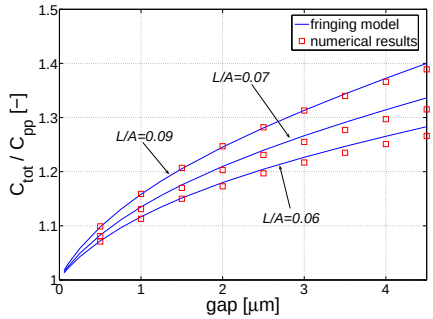

Figure 3: Fringing factor for various devices with different perimeter-to-area ratios L/A.

in which slip-flow and the effect of pressure on the gas mean free path is taken into account.

2.3 Contact Force

The modeling of contact is typically a compromise between physical realism (with a fundamental discontinuity when the surfaces make first contact) and numerical stability. Here, we let the contact force increase exponentially with decreasing separation between the rough surfaces [17], [18]. For numerical stability, smooth first order derivatives are created by applying a quadratic function in the transition from no contact to contact. This choice is rather arbitrary, but has no significant impact on the results. The contact force is implemented together with the spring force F_s through a contact force factor $k_n(z,r)$:

$$F_n + F_s = \frac{k}{k_n(z,r)} z \,, \quad (4)$$

with the factor $k_n(z,r)$ as shown in figure 4. The contact model only consists of one parameter r (roughness) that controls both the width of the contact region $w_c = r/4$ and the point of first contact $z_c = g - r$.

2.4 Membrane Bending

Membrane bending is a higher-dimensional problem that is, in general, not taken into account in other 1D

NSTI-Nanotech 2007, www.nsti.org, ISBN 1420061844 Vol. 3, 2007

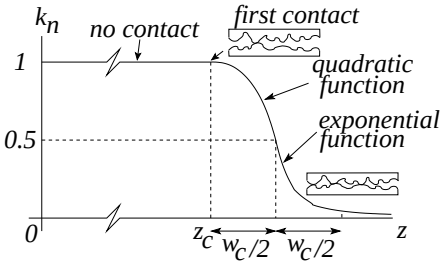

Figure 4: Contact force factor k_n as a function of the vertical displacement z, with a schematic representation of the contacting surfaces.

models (see table 1). Here, we treat this effect in a phenomenological way by introducing two model factors.

The first factor k_{fac} takes into account the effect of the bending of the membrane on the stiffness of the suspension. Due to the membrane bending, one side of the springs cannot be considered as a perfect guided-end. Instead, when the switch is open, the effective spring stiffness is reduced by a constant factor k_{fac} compared to the ideal (guided-end) situation:

$$(F_n + F_s)' = k_{fac} \frac{k}{k_n(z,r)} z \,. \tag{5}$$

The second factor $A_{fac}(z, z_c, z_1, z_2, A_1)$ models the influence of membrane bending on the effective capacitor area, and, as a result, capacitance and electrostatic force. This second model factor is schematically depicted in figure 5. The total corrected capacitance is calculated as:

$$C'_{tot} = C_{tot} A_{fac} \,, \tag{6}$$

which gives for the electrostatic force:

$$F'_{el} = \frac{1}{2} V^2 \left\{ A_{fac} \frac{dC_{tot}}{dz} + C_{tot} \frac{dA_{fac}}{dz} \right\} \,. \tag{7}$$

Parameter z_2 determines the point in the CV curve where partial-release becomes eminent, A_1 determines the capacitance value just before pull-out, and z_1 can be used to change the curvature of the capacitance-voltage (CV) characteristic in partial-release.

The model factors k_{fac} and A_{fac} constitute the only non-scalable part of the compact model.

2.5 Device Parasites

Next to the compact model, a separate parasitic network is developed for a switch in series configuration that includes the skin effect in the upper electrode, and a substrate node (figure 6). The skin effect is modeled by an equivalent fourth-order lumped L/R network [19] with adjusted parameter settings. No skin effect has to be taken into account for the lower electrode, because it is relatively thin compared to the penetration depth.

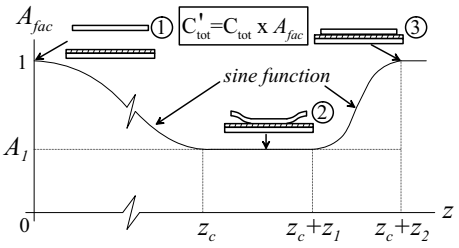

Figure 5: Model factor A_{fac} for the partial release effect, with a schematic representation of the membrane bending, with ① no membrane bending, ② partial contact, ③ fully closed contact.

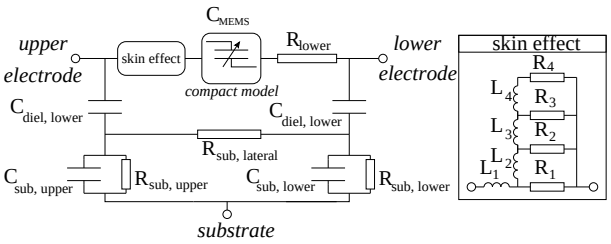

Figure 6: Parasitic network, including skin effect in the membrane. Parasitic paths lead from the upper electrode through the dielectric (abbrev. 'diel') towards the lower electrode and substrate (abbrev. 'sub').

3 RESULTS AND DISCUSSION

The six compact model parameters (g, r, k_{fac}, z_1, z_2, and A_1) can easily be extracted by manual tuning from static CV measurements. The parasitic network parameters are extracted by manual tuning from Sonnet simulations [20]. Figure 7 shows that our 1D model is capable of accurate modeling of the partial-release effect, and the pull-in and pull-out voltage. Transient closing times (figure 8) and S-parameter behavior of the model, embedded in RF test-interconnect (figure 9), show good correspondence with measurements. The modeling of transient opening times needs further improvement (figure 8) by a more accurate description of membrane bending and / or squeeze film damping. Envelope simulations are carried out to analyze the large-signal RF behavior of the switch. Self pull-in of the device on the RF signal is demonstrated. As an example, figure 10 shows the change in capacitance (upper panel) when an RF pulse of 1 GHz and 50 μs duration at 0 V DC bias is applied across the switch. The RF amplitude (lower panel) is chosen high enough to cause self pull-in (arbitrary units). The nonlinearity of the switch is studied in harmonic balance simulations. Figure 10 shows the third order intercept point (IP3) as a function of the tone spacing Δf in off-state. The graph reaches a minimum at the mechanical resonance frequency f_e (arbitrary units).

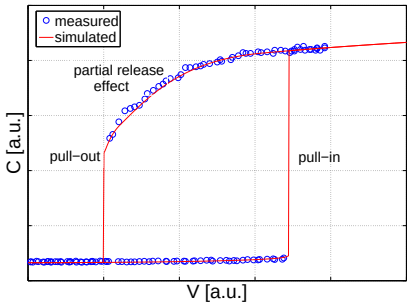

Figure 7: Simulation and measurement results for the (static) CV characteristic of an RF MEMS switch (arbitrary units).

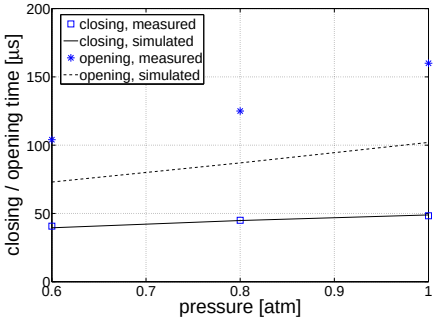

Figure 8: Simulation and measurement results for the closing and opening times of an RF MEMS switch at three different atmospheric pressures.

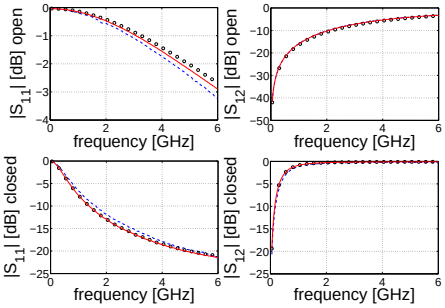

Figure 9: S-parameters for the compact model including parasites (solid lines), measurements (dashed lines), and Sonnet simulations (symbols) in off-state and on-state.

4 Conclusions

The presented model achieves a high level of accuracy, without the compromise of a loss of computational speed or ease-of-use in circuit simulators. The model includes a wide range of physical effects, such as fringing electrostatic fields, squeeze film damping, mechanical contact, and membrane bending. Validation on CV, transient, and S-parameter measurements shows good correspondence.

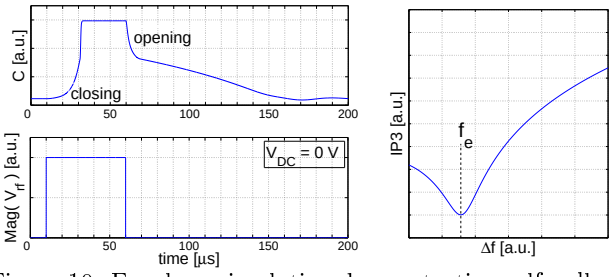

Figure 10: Envelope simulation demonstrating self pull-in (left). Harmonic balance simulation of the IP3 as a function of the tone spacing Δf (right).

REFERENCES

[1] S. Simion, IEEE CAS 2003 **1**, pp.125–128.

[2] L.A. Rocha *et al.*, 17th IEEE MEMS 2004, pp.249–252.

[3] J.B. Muldavin *et al.*, IEEE MTT-S MSD 2001 **3**, pp.2119–2122.

[4] G.M.H. Chan *et al.*, IEEE Int. Conf. on Robotics, Intelligent Systems and Signal Processing 2003 **2**, pp.698–701.

[5] S. Chowdhury *et al.*, J. Micromech. Microeng. **15**, pp.756–763 (2005).

[6] E.K. Chan *et al.*, IEEE MTT-S MSD 1997 **3**, pp.1511–1514.

[7] N. Iyer *et al.*, Sens. and Act. A **109**, pp.231–241 (2004).

[8] T. Veijola *et al.*, IEEE IMS 2002, pp.1213–1216.

[9] J.-M. Huang *et al.*, Sens. and Act. A **93**, pp.273–285 (2001).

[10] B. Schauwecker *et al.*, Sens. and Act. A **114**, pp.49–58 (2004).

[11] R. Batra *et al.*, J. Micromech. Microeng. **15**, pp.1175–1189 (2006).

[12] H.J. De Los Santos *et al.*, IEEE Microw. Mag. **5**, pp. 50-65 (2004).

[13] H.El. Kamchouchi *et al.*, Journal of Physics D: Applied Physics **8**, pp. 1365–1371 (1975).

[14] F. Stellari *et al.*, IEEE Transactions on Electron Devices **47**, pp. 222-231 (2000).

[15] G.K. Fedder, *Simulation of Microelectromechanical Systems*, Phd. Thesis, Univ. of California at Berkeley, 1994.

[16] P.G. Steeneken *et al.*, J. Micromech. Microeng. **15**, pp.176–184 (2005).

[17] J.A. Greenwood *et al.*, Proc. of the Royal Soc. Lon. A **295**, pp. 300–319 (1966).

[18] K.L. Woo *et al.*, Wear **58**, pp. 331–340 (1980).

[19] L.F. Tiemeijer *et al.*, IEDM 2003, pp.36.4.1–36.4.4.

[20] www.sonnetsoftware.com